Jet flow control at the blade scale to manipulate lift

Caroline Braud, Emmanuel Guilmineau

Jet flow control at the blade scale to manipulate lift

Caroline Braud, Emmanuel Guilmineau

Ecole Centrale de Nantes, LHEEA UMR CNRS 6598, 44321 Nantes, France

E-mail: caroline.braud@ec-nantes.fr

Abstract. The turbulent atmospheric boundary layer in which wind turbines are implemented is strongly inhomogeneous and unsteady. This induces unsteady mechanical loads at different characteristic time scales from seconds to minutes which limits significantly their life time. Different control strategies have been proposed in the framework of the French ANR SmartEole project to alleviate the impact of these upstream fluctuations at the farm, wind turbine and blade scales (i.e. characteristic time scales from seconds to minutes). The present work, which is part of this ANR project, focus on the flow control strategies at the blade scale, to manipulate lift and thus alleviate fatigue loads. The design of a $NACA65_4$-421 airfoil profile has been modified to be able to implement jet control. Slotted jet and discrete jet configurations were implemented numerically and experimentally respectivelly. Results show the ability of both configurations to increase the lift by up to 30% using a significant redistribution of the mean shear. Efficiency seems to be more important using slotted jets, which however needs to be confirmed from 3D simulations.

1. Introduction

In the last few decades many different flow control configurations (flat plates, ramps, bumps, ducts, airfoils, wind turbines ....etc) were investigated with different objectives depending on the application. They can be classified in two categories: circulation control and control of separated turbulent boundary layer flows.

The first category consist of using the ability of the flow to stay attached to a curved surface even when the main stream is perpendicular to it. Indeed, by blowing a tangential jet over a highly curved surface such as a rounded trailing edge of an airfoil, it is possible to move the rear stagnation point towards the lower surface of the wing by Coanda effect. This involves an increase of the circulation and its associated lift. A survey on circulation control can be found in [1]. This control strategy has been recently applied in the computational work of Djojodihardjo *et al* [2], who were using circulation control on a S809 airfoil to improve lift. The circulation control has also been applied on an elliptical airfoil to identify better the hierarchy of additional parameters affecting the flow [3] and to study the influence of blowing from a trailing-edge slot on the external flow [4].

The second control category, concerns the use of flow control to delay or prevent turbulent boundary layer separation. A survey on turbulent boundary layer flow control can be found in [5]. At first, passive devices such as small plates of different shapes (rectangular, triangular ...) inclined relatively to the free-stream velocity, often referred as Vortex Generators (VG), were mounted on the wall to generate streamwise vortices [6, 7, 8]. Many parameters such as location, geometry, arrangement, etc ... were shown to influence the control efficiency (see e.g. [8, 9]). The flow in which the VGs were embedded was also observed to influence the

dynamics of the produced vortices. Viscous diffusion causes the vortices to grow, the swirling velocity component to decrease and the boundary layer to develop towards a two-dimensional state [10]. The adverse pressure gradient is found to promote interactions between vortices, hence decreasing the control effectiveness [8]. Therefore, depending on the flow configuration (flat plate within an adverse pressure gradient, ramp, bump ...) and the initial conditions, the optimal set of control parameters varies.
Perturbations that arises on wind turbine blades can be viewed as a dynamic modification of the flow configuration (i.e. modification of the angle of attack in the wind tunnel framework, is equivalent to modify the adverse pressure gradient). To adapt the control to these perturbations and to be able to switch it off when it is not required, passive devices were rapidly replaced by active ones, which can be dynamically operated. Many active device types were developed whose source can strongly influence their nature[11]. When fluidic round jets are inclined relatively to the wall and to the main stream of the baseline flow, they are able to generate streamwise vortices qualitatively similar to those of passive VGs [12, 13]. Parametric investigations were performed to optimize their geometrical (orientation, spacing, etc.) and operating parameters (exit velocity, pulsating frequency, Duty Cycle...) [13, 14, 9]. By comparing slotted jet control configurations and discrete rounded jets control configurations, experimentally and numerically on the same configuration [15, 16, 17], it is found that the most efficient control is obtained when the structures resulting from the interaction of the control jet with the cross-flow (streamwise or spanwise), have a long enough coherence to reinforce the turbulent boundary subjected to an adverse pressure gradient.

In the present study, the design of a NACA65_4-421 airfoil profile has been modified (see figure 1) to adapt the lift to perturbations, by manipulating a separated turbulent boundary layer flow and taking advantage of Coanda effect from circulation control. A discrete squared jet flow control configuration and a slotted jet control configuration were performed, using respectively experiments and numerical simulations. Compared to previous studies, the present work is using a realistic blade profile shape and combine the experience of flow separation control with circulation control.

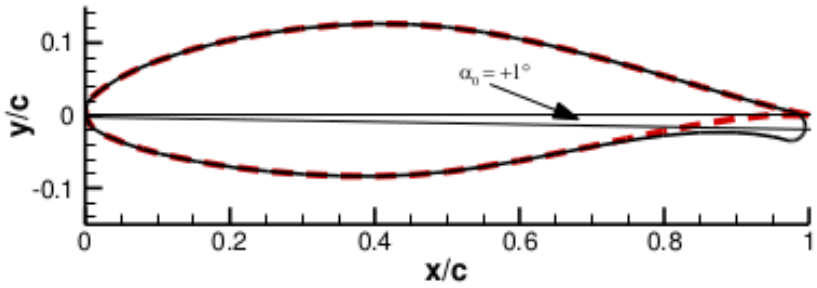

Figure 1. The trailing edge of a NACA65_4-421 airfoil profile has been rounded (radius of curvature 2%) and the camber of the airfoil has been adjusted to compensate aerodynamic degradation due to the round trailing edge. The original $\mathrm{NACA}65_4 - 421$ airfoil is in red dotted lines and the control profile $\mathrm{NACA}65_4 - 421\text{-CC}$ is in solid black line.

2. Experimental apparatus and instrumentation

2.1. Air delivery system

The air circuit, which was used to provide compressed air to the actuators, is composed of a compressor, a filtration system, a proportional valve and a volumetric flow meters (Q_v) which

serves to evaluate $C_\mu = \frac{Q_m U_{jet}}{P_\infty S}$ with Q_m the mass flow rate coefficient, P_∞ the free-stream dynamic pressure and $S = l.c$ (l is the span of the profile and c is the chord of the profile). This can be rewritten $C_\mu = 2.\frac{\rho_j Q_v U_{jet}}{\rho_\infty U_\infty^2 S}$ with U_∞ the free-stream velocity, ρ_j and ρ_∞ the density of the jet and the ambient air respectively. Because it was not possible to put a pressure probe in the plenum chamber, the jet exit velocity was evaluated using mass conservation from the volumetric flow meter to the jet exit velocity of a transverse line, assuming the jet is incompressible so that $\rho_j = \rho_\infty$. This leads to $U_{jet} = Q_v/S_j$ with $S_j = n_j \times D^2$, $n_j = 42$ the number of jets in a transverse line and D the squared jet section (see section 2.2). The momentum coefficient can thus be rewritten as follows:

$$C_\mu = 2.\frac{Q_v^2}{U_\infty^2 S S_j}$$

2.2. Jet control airfoil

In the present study the NACA65$_4$-421-CC profile has been specifically designed to be able to implement control jets around its surface. It is made of a stack of 2D profiles of two different types, named "blind" and "non-blind" profiles (figure 2a).

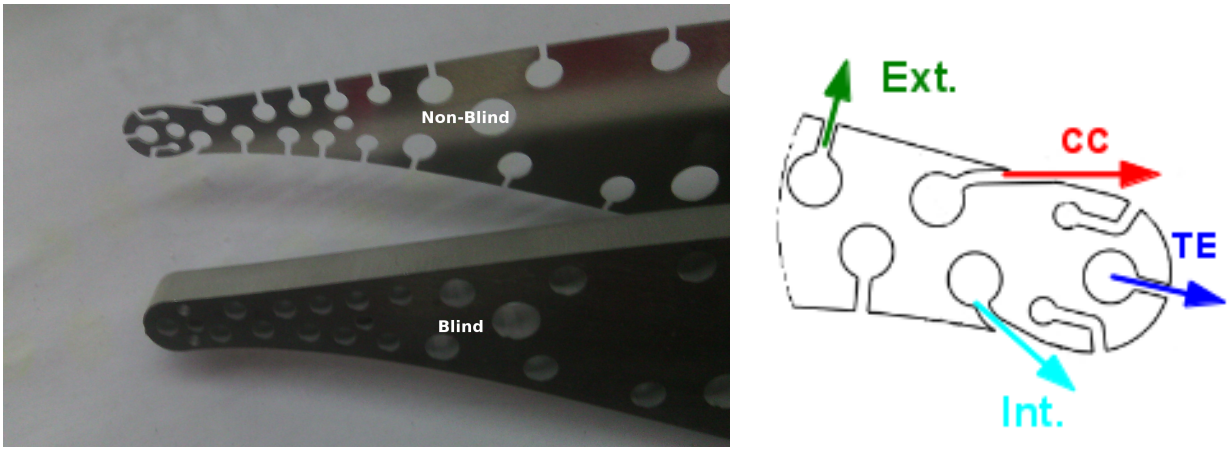

a) b)

Figure 2. a) Samples of a blind and a non-blind NACA65$_4$-421-CC profile, b) Examples of jet control possibilities from this design: blowing for Circulation Control (CC: red arrow), Trailing Edge blowing (TE: blue arrow), Intrados blowing (Int: cyan arrow), Extrados blowing (Ext.: green arrow)

Blind profiles (10 mm width) are made of 42 independent holes distributed along the airfoil's interior. Non-blind profiles (1mm width) are made of similar holes with, for each, an hole opening onto the airfoil's surface. The stack of these 2D profiles provides a plenum chamber in the transverse direction that can be connected indifferently by a compressed air system or by a pressure manometer. The non-blind profiles are sandwiched by 2 blind profiles on each side, so that providing a squared surface hole of diameter $D = 1$mm. The distance between the center of two squared holes is $\lambda = 21$mm. With this design, it is possible to blow transverse lines of squared jets independently around the airfoil's profile (see examples in figure 2b). In the present study, only the transverse line at the trailing edge (red arrow of figure 2b) was provided with air from both ends of the airfoil. Other transverse lines were used for surface pressure measurements (see section 2.4). The final length of the profile is $l = 1.1$ meter and its chord is $c = 0.3$ meter.

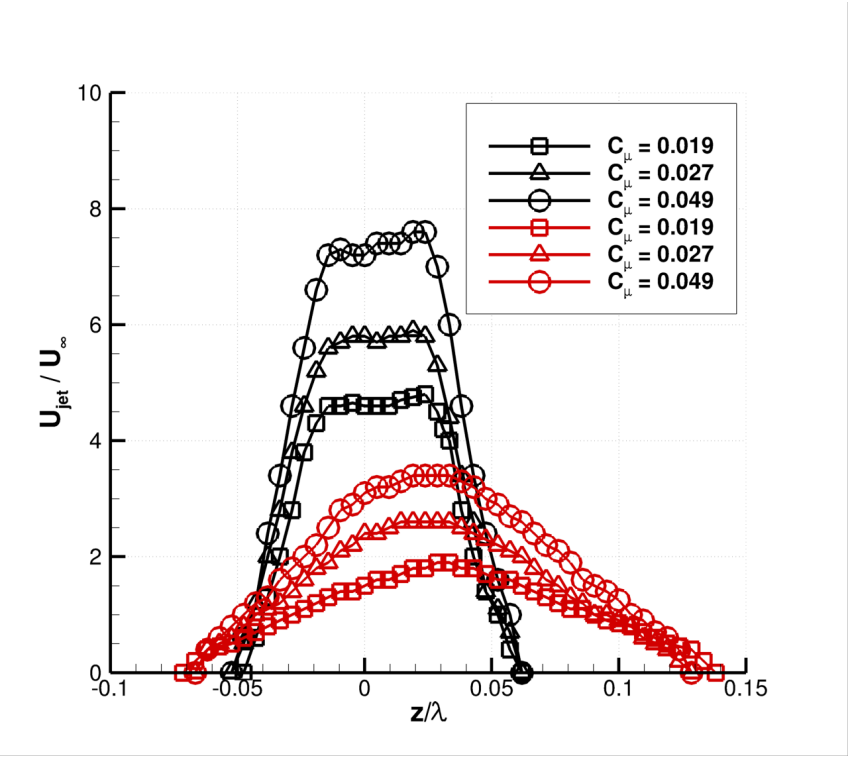

Figure 3. Mean jet control profiles at x/c=0.965 and y/c=0 (black lines) and at x/c=1.01 and y/c=0.0075 (red lines)

The framework of the present study is as follows: x is the streamwise direction, the spanwise direction y is perpendicular to the blade's span and positive values are towards the wind tunnel ceiling, z is the spanwise direction along the span of the blade and is chosen to have a direct coordinate system. The origin is taken at the leading edge of the profile, at approximately the middle of the blade's span in z direction, so that it is at the middle of a non-blind profile (i.e. one end of the profile is located at $z = 539mm$).

To be able to understand how the control jet evolves without cross-flow, the control jet was first characterized alone on bench experiments. A home made total pressure probe (P_t) with an external diameter of 500 μm (internal diameter of 250 μm) was used. It was placed on a 3D micro-displacement system with its axis in the streamwise direction. The probe was then connected to a Furness manometer through Tygon tubes. It was assumed that the exit of the controlled jet is incompressible, so that the static pressure is equal to the ambient pressure (P_o). The control jet homogeneity was checked at $x/D = 2$ by displacing the pressure probe at the maximum value of the control jet exit velocity in y and z directions. Results exhibit a standard deviation of the control jet exit velocity, U_{jet}, of 13% in the z direction. Also, the mean spatial organization of a single jet was characterized at $z/\lambda = 0$. In the chosen framework defined previously, this corresponds to the location of PIV measurements (i.e. around the center of the profile's span). The jet is found to be slightly deviated in z and y directions (3% of λ and 1.4% of λ respectively). Then, it is clear that the control jet velocity strongly decreases with the streamwise direction. For $C_\mu = 0.019$, it decreases from the velocity ratio $VR = U_{jet}/U_\infty = 4.5$ at $(x/c, y/c) = (0.965, 0)$ to $VR = 2$ at $(x/c, y/c) = (1.010, 0.0075)$ (see figure 3b). The jet was characterized with different momentum coefficients. Results show that only the jet amplitude is modified, with no significant additionnal deviations of the jet.

2.3. Wind tunnel facility

The measurements were conducted at the University of Orléans, in the Lucien Malavard closed return wind tunnel of the PRISME laboratory. It has a section test of 5 m long with a cross-section of 2 m x 2 m. The turbulence level in this test section is below 0.4 %. In the present study, the operating speed of the wind tunnel was $U_\infty = 10$m/s. The 2D blade was mounted between two vertical flat planes in order to achieve a 2D flow configuration.

2.4. Surface pressure measurements

The pressure distribution around the profile was measured with a 32- channel and a 16 channel differential pressure scanners ESP-32HD (GE, 1PSI range) embedded in a MicroDaq system (SHELL). The reference pressure is the static pressure in the test section, measured close to the upper wall of the test section, at the blade location.

2.5. Balance measurements

The airfoil was mounted on both tips onto a 6-component platform balance used for time-averaged lift and drag measurements and located under the test section. The balance was carefully calibrated and lift and drag coefficient uncertainties were estimated to be less than 2 %.

2.6. Particle image velocimetry

Mean velocity fields around the airfoil trailing edge were studied from 2D PIV measurements in order to analyze flow topology with and without jet control in longitudinal planes of the airfoil model. In order to characterize the control effect from the discrete control jets, 2D PIV planes were acquired at different spanwise locations. The PIV system consisted in a Nd:Yag laser (2x200mJ) emitting pulses with a 2.5Hz emission rate. Seeding particles were made of micro-sized olive oil droplets spayed by a PIVTEC seeding system. Images were acquired with a LaVision Imager LX camera (4032px x 2688px) and a 200mm lens. The final resolution is of one vector every 0.8mm, with a $32 \times 32px^2$ interrogation window. One thousand image pairs were recorded. Vector field were computed using OpenPIV Software running in parallel [18]. A signal to noise ratio of 1.3 and a threshold filter on velocity components were used to validate the vector field.

3. Numerics

3.1. Flow solver

The solver ISIS-CFD, available as a part of the FINE$^{\text{TM}}$/Marine computing suite, is an incompressible unsteady Reynolds-averaged Navier-Stokes method mainly devoted to marine hydrodynamics. The method features several sophisticated turbulence models: apart from the classical two-equations k-ε and k-ω models, the anisotropic two-equation Explicit Algebraic Reynolds Stress Model (EARSM), as well as Reynolds Stress Transport Models (RSTM), are available [19]. All models are available with wall-function or low-Reynolds near wall formulation. Hybrid LES turbulence models based on Detached Eddy Simulation (DES) are also implemented and have been validated on automotive flow characterized by large separation [20]. Additionally, several cavitation models are available in the solver.

The solver is based on finite volume method to build the spatial discretization of the transport equations. The unstructured discretization is face-based. While all unknown state variables are cell-centered, the system of equations used in the implicit time stepping procedure are constructed face by face and the contribution of each face is then added to the two cells next to the face. This technique poses no specific requirements on the topology of the cells. Therefore, the grids can be completely unstructured: cells with an arbitrary number of arbitrarily-shaped

faces are accepted. Pressure-velocity coupling is enforced through a Rhie & Chow SIMPLE type method: at each time step, the velocity updates come from the momentum equations and the pressure is given by the mass conservation law, transformed into a pressure equation. In the case of turbulent flows, transport equations for the variables in the turbulence model are added to the discretization.

Free-surface flow is simulated with a multi-phase flow approach: the water surface is captured with a conservation equation for the volume fraction of water, discretized with specific compressive discretization schemes [21]. The technique included for the 6 degrees of freedom simulation of ship motion is described by Leroyer & Visonneau [22]. Time integration of Newton's law for the ship motion is combined with analytical weighted analogy grid deformation and rigid motion to adapt the fluid mesh to the moving ship. To enable relative motions of appendages, propellers or bodies without having recourse to overlapping grids, a sliding grid approach has been implemented. Propellers can be modeled by actuator disc theory, by coupling with boundary element codes (RANS-BEM coupling [23]) or with direct discretization through e.g. the rotating frame method or sliding interface approaches. Finally, an anisotropic automatic grid refinement procedure has been developed which is controlled by various flow related criteria [24]. Parallelization is based on domain decomposition. The grid is divided into different partitions, which contain the cells. The interface faces on the boundaries between the partitions are shared between the partitions; information on these faces is exchanged with MPI (Message Passing Interface) protocol. The method works with the sliding grid approach and the different sub-domains can be distributed arbitrarily over the processors without any loss of generality. Moreover, the automatic grid refinement procedure is fully parallelized with a dynamic load balancing working transparently with or without sliding grids.

The actuation is implemented as boundary conditions. The velocity is imposed on the jet boundary as $\mathbf{U} = \mathbf{U}_{jet}$ and the direction of the jet is perpendicular to the boundary.

3.2. Numerical simulation set-up

The numerical simulations are 2D simulations. The computation domain starts $2c$ before the airfoil and extends $5c$ behind the airfoil. The height of the domain is $6c$ and the profile is centered in the domain. The mesh is generated using Hexpress, an automatic mesh generator. This software generates meshes containing only hexahedrals. For the surface of the airfoil, a no-slip condition boundary condition is used and the wall normal resolution is $y^+ \leq 0.5$. The mesh consists of 160532 cells and the profile is described by 8266 faces, see figure 4. The turbulence model used in this study is the $k - \omega$ SST of Menter [25].

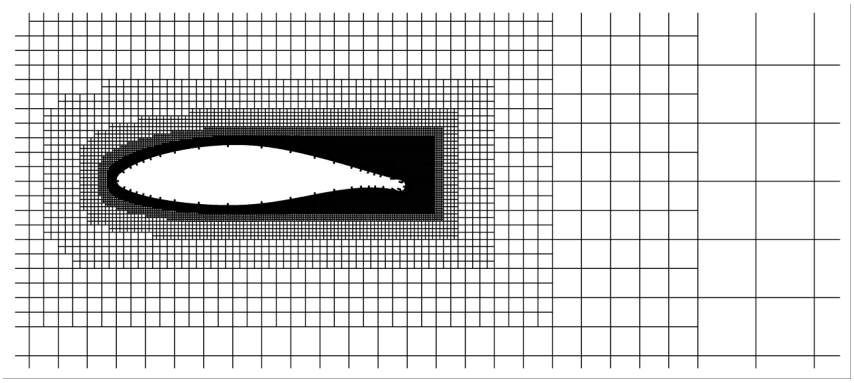

Figure 4. Initial mesh

For this study, the simulations have been done with an automatic adaptive grid refinement.

In this case, the refinement criterion used is based on the flux component Hessian and the minimum cell size is 0.1 mm. The meshes obtained consists of 169435 cells for the angle of attack $\alpha = 0°$ and 174809 cells for the angle of attack $\alpha = 5°$. Both meshes are presented in figure 5.

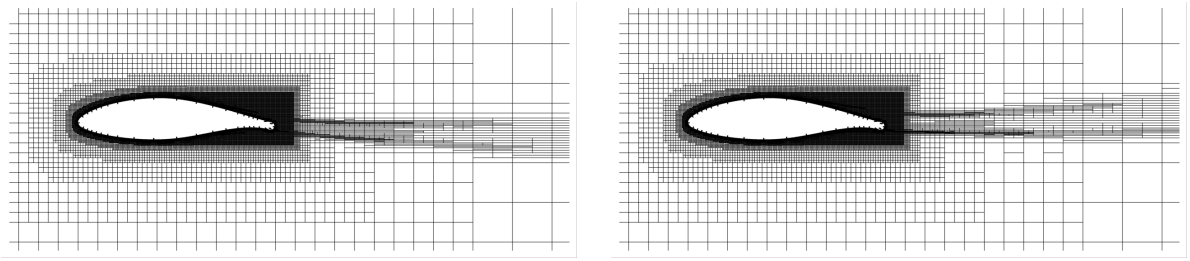

(a) 0 degree (b) 5 degrees

Figure 5. Refined meshes

4. Baseline results

4.1. Validation of the jet control airfoil

The jet control airfoil is an unusual design and needs to be validated with results from a similar blade shape without implementation of control which is available at the PRISME laboratory. First, balance measurements of both profiles were performed and compared (see figure 6a). Results show that the jet control airfoil is only slightly modified at high angle of attack, when a flow separation occurs at the trailing edge (i.e. $\alpha > 6°$). The present control objective is to modulate lift when the flow is still attached (i.e for angle of attack around $3 < \alpha < 5°$), the jet control airfoil can thus be validated. Pressure measurements around the chord in the jet control airfoil is obtained using the pressure integration of surface squared holes (diameter $D = 1$mm) in each transverse line. To validate this unusual procedure, pressure measurements were measured against pressure measurements from the PRISME airfoil (see for example figure 6b). At last, the effect of the chord based Reynolds number on the lift coefficient was investigated from $Re_c = 200k$ to $Re_c = 800k$ which highlights that the lift coefficient is mainly affected at high angles of attack.

4.2. The baseline results

To be able to compare the slotted jet configuration from numerical results with the discrete squared jet configuration from experiments, a first step is to compare the baseline flow. As can be seen in figure 7a, differences in the lift coefficient are mainly present at high angle of attack with a slight lift overestimation with numerical simulations. This lift difference could be attributed partly to the slight lack of experimental measurements points from pressure taps when peak occurs (see figure 7b). Another part of these slight differences may also be attributed to the integration of 3D effect with the unusual way to obtain pressure measurements experimentally.

At last, the spatial organization is compared (see figure 8). As it can be seen, experimental results exhibit a thicker wake, a smaller velocity deficit area with its center oriented more towards the negative y/c direction. However, the topology is retrieved, with one main recirculation zone that is highlighted by the roll-up of the streamlines in the velocity deficit area.

These results are found sufficient to compare control effect presented below.

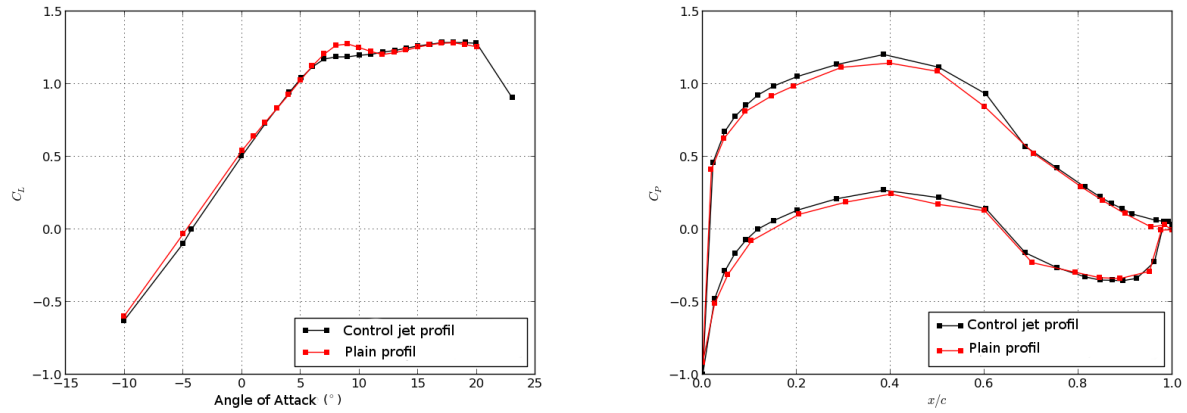

a) b)

Figure 6. Validation of the jet control airfoil ($Re_c = 20k$): a) the lift coefficient obtained from balance measurements, b) the pressure coefficient at $\alpha = 2°$ of angle of attack.

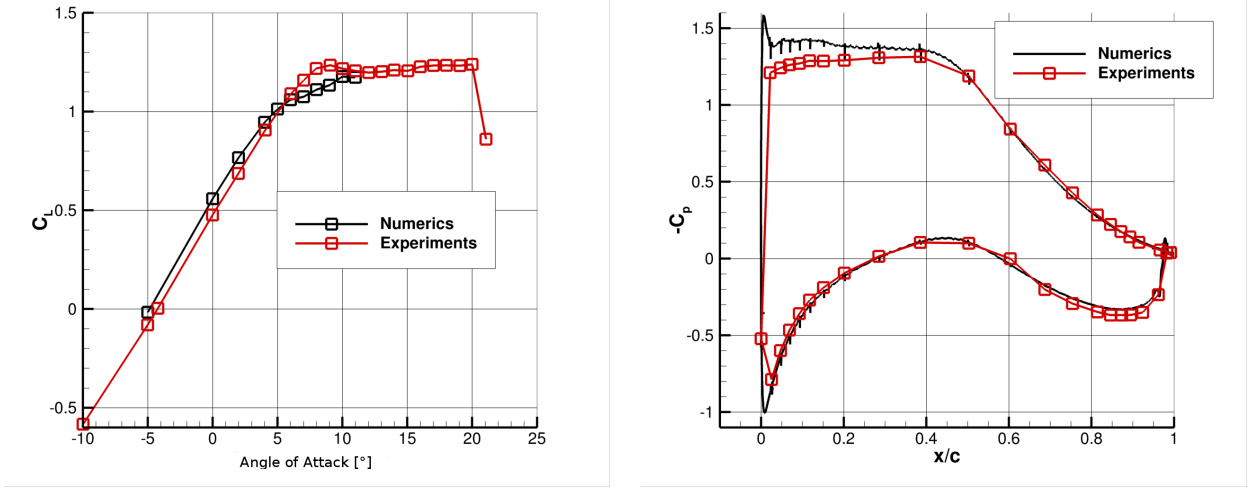

a) b)

Figure 7. Comparison of baselines configurations at the angle of attack of $\alpha = 5°$ and $Re_c = 200k$: a) Lift coefficient b) Pressure coefficient

5. Slotted jets versus discrete squared jets

Because simulations are 2D, the control can be viewed as a 2D slot jet actuation. Slot jets and discrete jets clearly act differently (see e.g. [16] and [15]). Slot jets generate vortices with a tranverse axis while discrete jets generate streamwise vortices. Therefore, once simulations are validated without control, main differences between 2D simulations and experiments come from differences in the control action. However, it is important to note that most of experimental works have to deal with reality when trying to implement a control set-up. In particular,

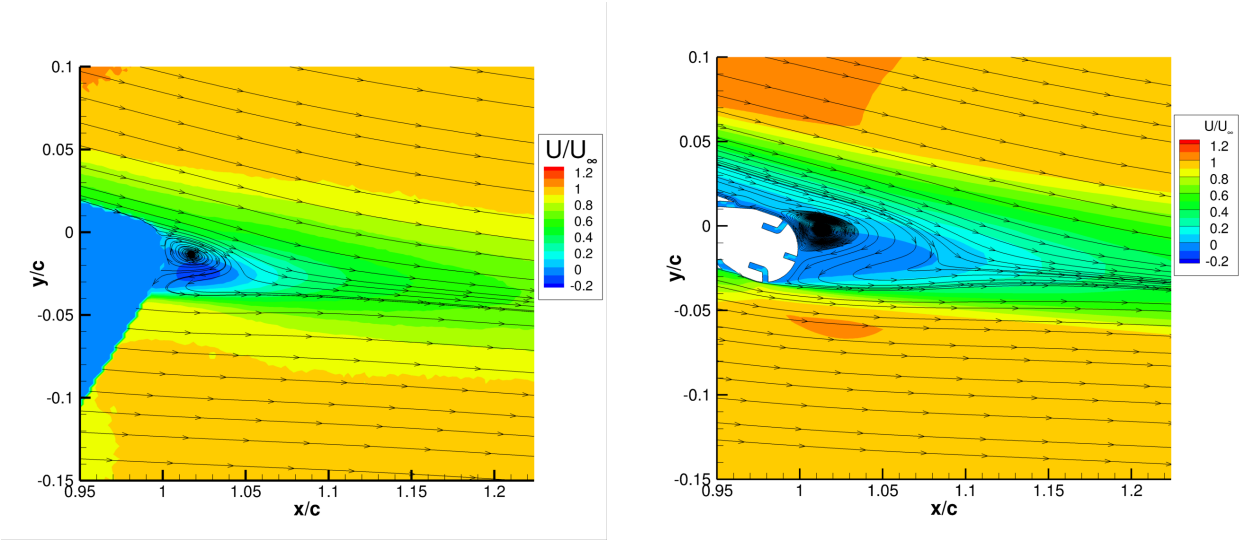

a) b)

Figure 8. Comparison of baseline configurations using isocontour of the streamwise velocity with streamlines superimposed, at the angle of attack of $\alpha = 5°$ and $Re_c = 200k$: a) PIV measurements, b) Numerical simulations

actuators have their own dynamics [11, 26, 27] and the way they are implemented can significantly modify the control [28, 29]. It is generally too difficult to take into account these additional parameters in numerical works, so that the comparison between slot and discrete jets efficiency has to be taken carefully. Future work will include a simulation on the discrete squared jet configuration to validate comparisons between numerical and experimental studies of the present configuration.

5.1. Lift manipulation

First balance measurements were performed at a fixed angle of attack for 9 C_μ. Then 4 C_μ were chosen and balance measurements were performed at 5 selected angles of attack ($\alpha = 0$, 2°, 4°, 6° and 8°). Numerically, 7 C_μ were performed at a fixed angle of attack. By increasing the moment coefficient of the jets, we are able to increase the gain of the lift ΔC_L whatever the jet configuration and whatever the angle of attack of the profile (see figure 9). The gain can goes up to 30%. From these results, slotted jets are more efficient than discrete squared jets. However this conclusion should be taken carefully as we are not sure to be able to reproduce the controlled jet imposed numerically. Another important remark is the non-linearity of this gain which is retrieved in both configurations below $C_\mu \simeq 0.025$. Some angles of attack of the profile are even non-monotonic (see e.g experimental results with an angle of attack $\alpha = 2°$ and $\alpha = 4°$). In practice, this will prevent the implementation of a simple proportional feedback loop.

5.2. Mean shear effect

The mean spatial organization is analyzed to be able to understand how jets are able to manipulate the lift and what are the differences between configurations. All results from

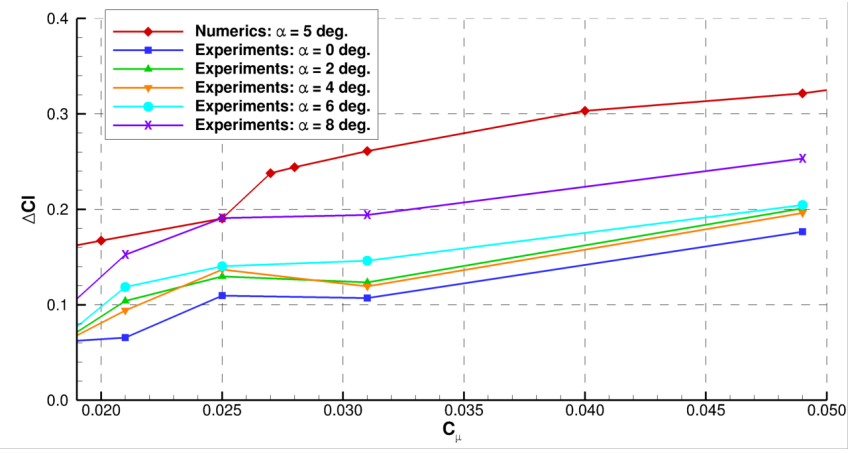

Figure 9. The lift gain $\Delta C_L = C_{L0} - C_{Lwc}$ with C_{L0} the lift coefficient without control and C_{Lwc} the lift coefficient with control.

the discrete jet presented in this section are located at the center of a jet to be able to compare with slotted jets. First results clearly show that the jets significantly modify the mean spatial organization (see figure 10). Remarkably, the peaks value of the streamwise velocity are approximately of the same order of magnitude $U/U_\infty = 1.8$, while initial values of the imposed jet are significantly different: $VR = 6$ at $x = 2D$ for squared jets (see figure 3) and VR is imposed to 2 in the hole of slotted jets.

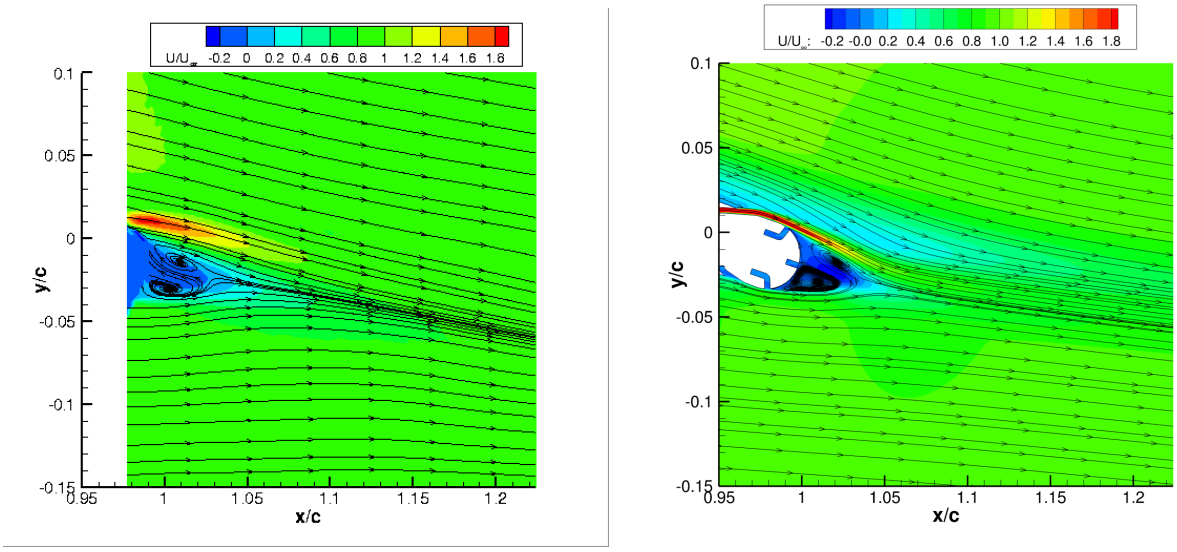

a) b)

Figure 10. Isocontour of the streamwise velocity with streamlines superimposed for a control case ($C_\mu = 0.027$) from both configurations: a) discrete squared jets or b) slotted jets

By looking more carefully on y profiles at two streamwise distances (see figure 10), the slotted jet exhibit a significantly different mean shear than the discrete squared jets. Indeed, the peak width of the streamwise velocity is much thinner in the slotted configuration, and is accompanied

with a much stronger deceleration in the positive y/c direction. We can define the strength of the shear obtained from the control jets by the ratio between the acceleration's peak and the deceleration's peak. In that case, the strength of the slotted control is almost twice the one with squared jets. When evolving downstream, the shear area of the slotted case is significantly decreased and displaced towards negative y/c, in good agreement with the modification of the jet trajectory of figure 11b. For the discrete squared jet control, the shear is only slightly displaced towards negative y/c and it is slightly larger in good accordance with the spreading of the controlled jet of figure (see figure 11a).

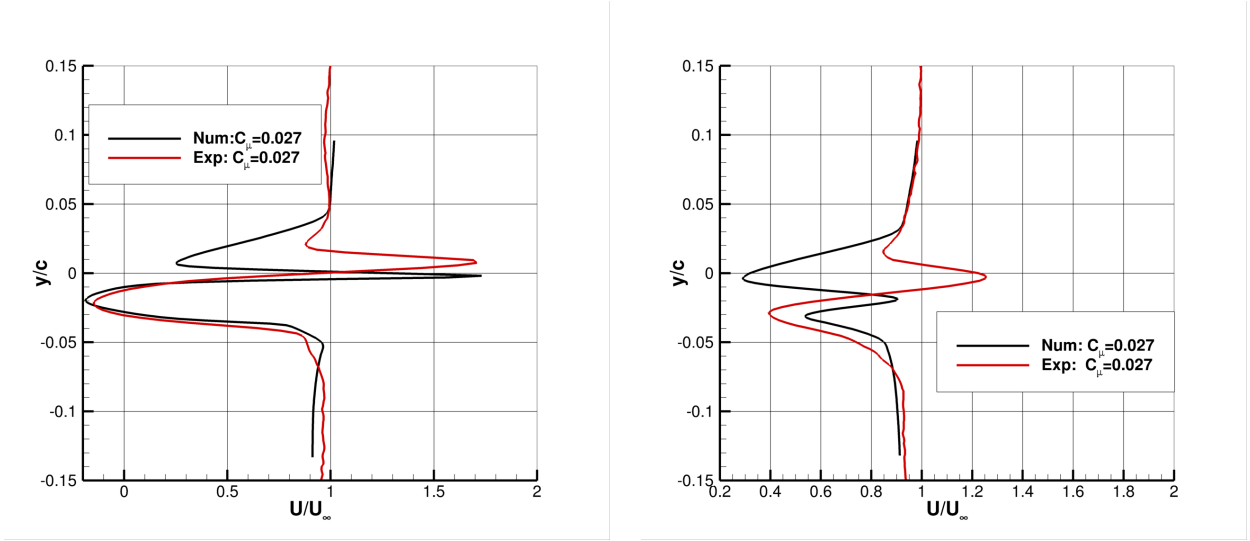

a) b)

Figure 11. Y profiles of the mean streamwise velocity at two streamwise distances $x/c = 1.01$ and $x/c = 1.05$ for both control configurations: a) discrete squared jets b) slotted jets

5.3. Influence of C_μ

It is now interesting to analyze how the control efficiency increases with C_μ for both control jet configurations. Increasing the momentum coefficient C_μ proportionally increases the shear locally in both controlled configurations as it is highlighted in figures 12 and 13. Again, the effect of slotted jet is more efficient then the one from discrete squared jets with an increase of the strength of the shear almost 10% higher.

5.4. Discrete squared jets

Previous results were presented at $z/c = 0$, while discrete squared jets have the spanwise action of the control. Figures 14 should be compared to the baseline flow of figure 8. Remarkably, a complete suppression of the mean separation flow can be observed at $z/c = 0.33$ while the jet strength can only be seen at $z/c = 0$ and slightly at $z/c = 0.43$. This moderates the previous analyzes. Indeed, even if slotted jet control exhibit a better efficiency, it was not possible to suppress the flow separation. At last, on can note that the efficiency of discrete squared jets is outside the influence of the jet control alone (see figure 3). This has to be related to the longitudinal vortices produced behind controlled jets which are generally located near the shear between the controlled jet and the cross-flow [12]. Unfortunately, present results cannot exhibit such vortices that should be measured in $x - z$ planes.

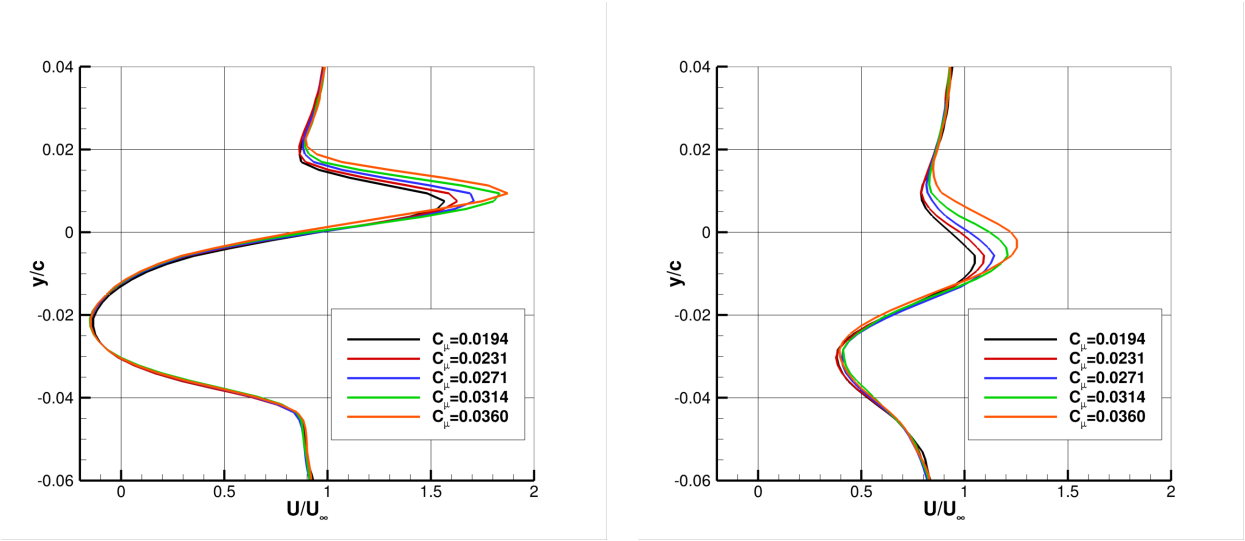

a) b)

Figure 12. Y profiles for the discrete squared jet control configuration at $z/c = 0$ and: a) $x/c = 1.01$ b) $x/c = 1.05$

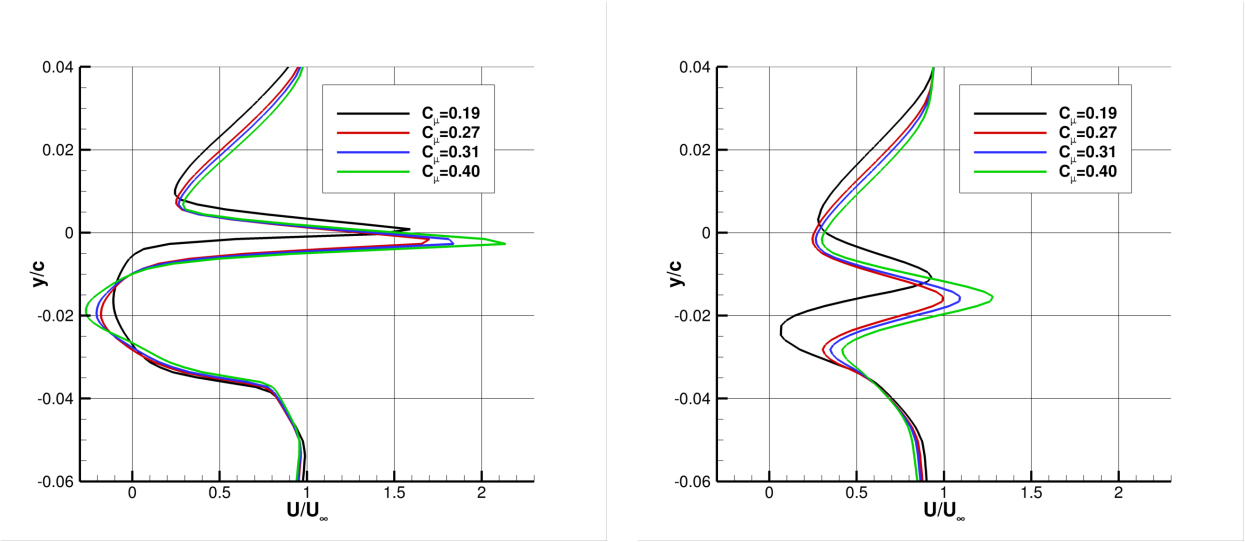

a) b)

Figure 13. Y profiles for the slotted jet control configuration at: a) $x/c = 1.01$ b) $x/c = 1.05$

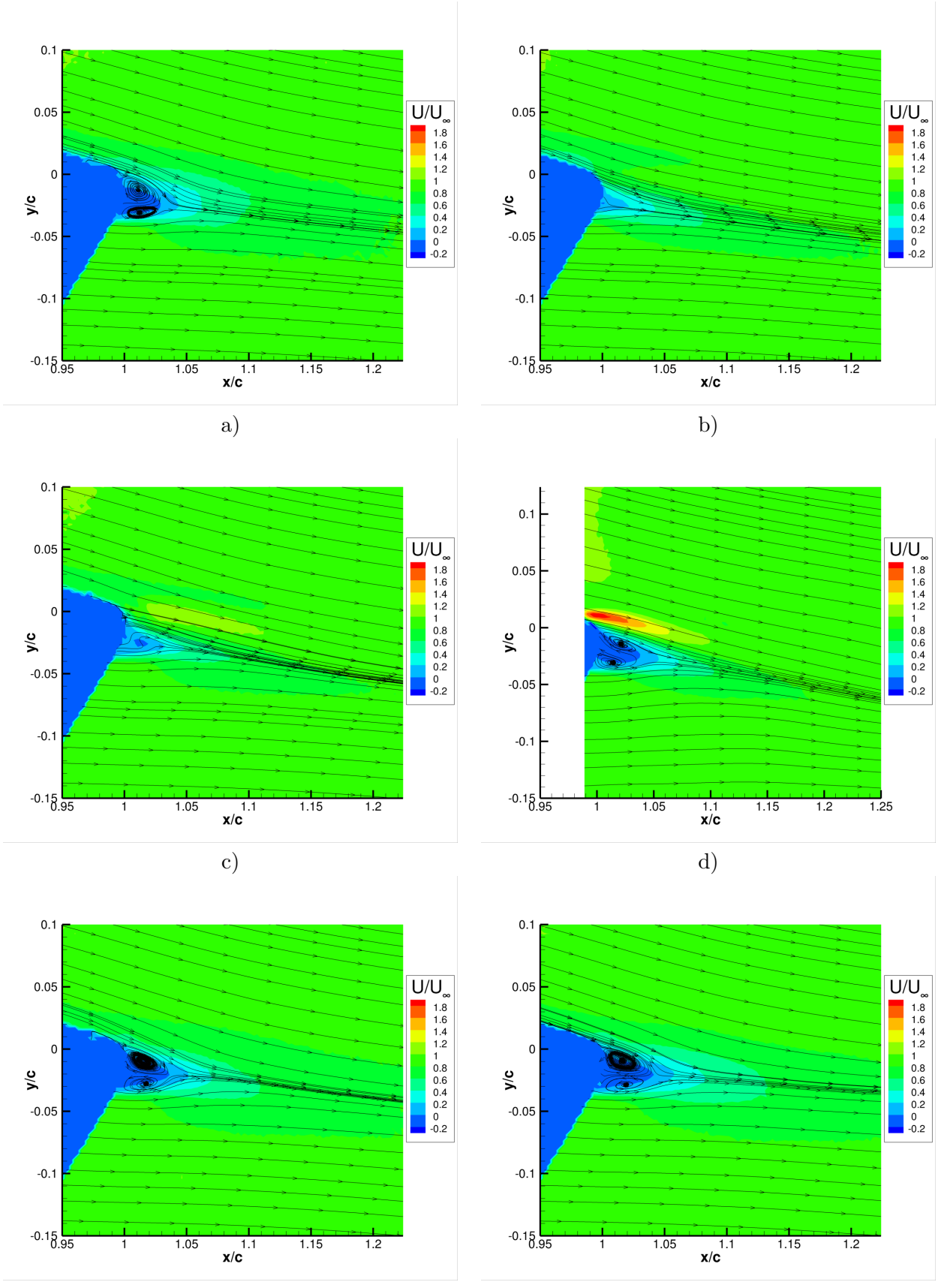

Figure 14. 2D-2 components PIV planes in the tranverse direction of the discrete squared jet configuration, for $C_{mu} = 0.027$: a) $z/\lambda = 0.43$ b) $z/\lambda = 0.33$ c) $z/\lambda = 0.14$ d) $z/\lambda = 0$ e) $z/\lambda = -0.19$ f) $z/\lambda = -0.33$.

5.5. Conclusion/Perspectives

This study presents the results of jet flow control to manipulate the lift of a realistic modified 2D wind turbine blade ($NACA65_4$-421 profile) with the objective to alleviate loads from atmospheric flows. Two control configurations were investigated in term of lift gain and mean spatial organization. The first one is a slotted jet control configuration obtained from a 2D simulation. The second one is a discrete squared jet control configuration from experiments. Both configurations were able to manipulate the lift. A lift gain up to 30% could be obtained with "a priory" more efficiency when using the slotted jet configuration. However, these results should be moderated by the fact that there is still a doubt on reproducing experimentally such a numerical controlled jet (additional losses due to tubing arrangement, energy to provide for the mass flux needed ...). Also, it was found that only the discrete squared jet configuration was able to completely suppress the flow separation on the side of the controlled jet. Future work will perform 3D simulations to compare the discrete squared jet configuration with experiments. This will help to remove the doubt on how to generate realistic controlled jets numerically and will provide a useful tool to investigate a distributed control action.

References

[1] Joslin R D and Jones G S (eds) 2006 *Application of Circulation Control Technology* vol 214 (American Institute of Aeronautics and Astronomics, Inc.)
[2] Djojodihardjo H, Hamid M F A, Jaafar A A, Basri S, Romli F I, Mustapha F, Rafie A S M and Majid D L A A 2013 *Journal of Renewable Energy* **2013** Article ID 839319
[3] Chen C, R Seele R and Wygnanski I 2012 *AIAA journal* **50** 2235–2247
[4] Wetzel D, Griffin J and Cattafesta L 2013 *Journal of FLuid Mechanics* **730** 99–144
[5] GadelHak M 2000 *Flow Control : passive, active and reactive flow management* (Cambridge)
[6] Shabaka I, Mehta R and Bradshaw P 1985 *J. of Fluid Mech.* **155** 37–57
[7] Schubauer G and Spangenberg W 1960 *J. of Fluid Mech.* **8** 10–32
[8] Lin J 2002 *Progress in Aerospace Sciences* **38** 389–420
[9] Godard G and Stanislas M 2006 *Aerospace Science and Technology* **10** 455–464
[10] Angele K and Muhammad-Klingmann B 2005 *European Journal of Mechanics B/Fluids* **24** 539–554
[11] Cattafesta L and Sheplak M 2011 *Annual Review of Fluid Mechanics* **43** 24772
[12] Cathalifaud P, Godard G, Braud C and Stanislas M 2009 *Journal of turbulence* **10**
[13] Compton D and Johnston J 1992 *AIAA Journal* **30**
[14] Khan Z and Johnston J 2000 *Int. J. of Heat and Fluid Flow* **21** 506–511
[15] Laval J, Braud C, Fournier G and Stanislas M 2010 *J. of Turbulence* **11**
[16] Fournier G, Laval J, Braud C and Stanislas M 2010 *Int. J. of Flow Control* **2** 289–310
[17] Cuvier C, Braud C, Foucaut J and Stanislas M 2011 *7th Turb. and Shear Flow Phenomena* (Ottawa - Canada)
[18] Taylor Z J, Gurka R, Kopp G A and Liberzon A 2010 *IEEE Transactions on Instrumentation and Measurement* **59** 3262–3269
[19] Deng G D and Visonneau M 1999 *7th Symposium on Numerical Ship Hydrodynamics* (Nantes, France) pp 4.4–1–15
[20] Guilmineau E, Deng G B and Wackers J 2011 *Journal of Fluids and Structures* **27** 807–816
[21] Queutey P and Visonneau M 2007 *Computers and Fluids* **36** 1481–1510
[22] Leroyer A and Visonneau M 2005 *Journal of Fluids and Structures* **20** 975–991
[23] Deng G B, Queutey P, Visonneau M and Salvatore F 2013 *MARINE 2013, International Conference on Computational Methods in Marine Engineering V* ed Brinkmann B and Wriggers P pp 541–551
[24] WAckers J, Guilmineau E, Palmieri A and Queutey P 2014 *Proceedings of 17th Numerical Towing Tank Symposium (NuTTS) 2014* (Marstrand, Sweden)
[25] Menter F 1994 *AIAA Journal* **32** 1299–1310
[26] A A Lockerby P W Carpenter C D 2007 *Flow Turbulence and Combustion* **78** 205–222
[27] Braud C and Dyment 2012 *Physics of Fluids* **24**
[28] Warsop C, Hucker M, Press A and Dawson P 2007 *Flow Turbulence and Combustion* **78** 255–281
[29] Peterson S D and Plesniak M W 2004 *Journal of fluid mechanics* **503** 57–91

Acknowledgments
This project is partly funded by the national French project SMARTEOLE (ANR-14-CE05-0034). Authors would like to thanks Rodrigue LOISIL for the design of the experimental blade. Also, experiments at PRISME Laboratory could not be performed without the help of Sophie BALERIOLA and Stephane LOYER and the support of Sandrine AUBRUN and Annie LEROY.